7. RADIATION BACKGROUND AND RELATED EFFECTS

The most critical problem faced by the satellite, and consequently also impacting on its operations, was the radiation environment in the geostationary transfer orbit. The regular crossings of the van Allen radiation belts meant that the satellite was repeatedly exposed to very high proton and electron radiation levels, much higher than those for which the satellite and payload were designed. The radiation damage resulted in the progressive degradation of the solar array performance (described in Chapter 11), heater anomalies (Chapter 12), the failure of the gyroscopes (Chapters 13–16), and eventually the loss of the mission through failure of the telecommunication subsystem. In addition, the radiation environment was responsible for an increased star mapper signal background which complicated and degraded the real-time attitude determination, as well as the Tycho data analysis.

7.1. Introduction

The Hipparcos payload was known and predicted to be sensitive to background signals induced by energetic electrons and protons. Radiation effects were an important consideration even in the planned geostationary orbit, and careful analysis of the focal plane shielding was made before launch.

After the failure of the apogee boost motor to raise the satellite into its planned orbit, there was concern that the considerably harsher radiation environment of geostationary transfer orbit would severely limit the mission lifetime due to solar cell degradation or component failure. It is likely that the eventual failure of four out of five gyroscopes was due to radiation damage to control electronics. There was an additional initial concern that the background signal induced in the telescope systems by energetic particle hits on the optics or the photomultiplier detectors would strongly limit the possible observation time during the orbit.

This chapter provides a summary of the radiation environment in near-Earth orbit, and details the effects of the radiation background on the satellite. From the perspective of understanding the radiation environment in geostationary transfer orbit, the Hipparcos observations over the mission lifetime yielded a long-term data set which strongly reflects the structure of the radiation belts, their dynamics and the effects of solar particle events.

7.2. The Radiation Environment in Space

The space radiation environment presents a hazard to most satellite missions, irrespective of the orbit. There are many high-energy particle populations in the different regions of space which can cause damage to spacecraft and instrument components. In addition they can give rise to detector interference, single-event upset and electrostatic charging.

Some regions, however, pose more of a threat to satellite experiments than others. For example, the trapping of charged particles, in particular electrons and protons, by the Earth's magnetic field, creates the toroidal radiation belts known as the van Allen belts. As a consequence of being in geostationary transfer orbit Hipparcos crossed the van Allen belts slightly more than four times per day. The inner belt, between 1000 and 4000 km from the Earth's surface, contains mainly high-energy protons, while the outer belt between 8000 and 12 000 km, contains high-energy electrons. The degradation of directly exposed subsystems, e.g. solar generators and electronic equipment, are important because of repeated exposure to radiation. Out of the van Allen belts, radiation rates are caused by particle events and galactic cosmic rays, and these can induce single event upsets.

During the early part of the mission, the effects of the radiation background on the solar array performance was considered to be a crucial factor in the overall satellite lifetime, and a particular effort was therefore devoted to understanding and predicting the solar array in-orbit power loss due to radiation damage. In practice, this was based on a correlation of laboratory solar-cell radiation damage data with an estimate of the radiation dose for the anticipated spacecraft trajectory. This estimate, therefore, also required an accurate knowledge of the spacecraft flight path exposure to the Earth's charged-particle trapping domains.

Steady improvements and refinements to our knowledge of the magnetosphere have been made since the discovery of the van Allen radiation belts in 1959. Static trapped-particle-environment models have evolved to the point where spatial and temporal variations may be allowed for. The radial electron and proton flux profiles depicted in Figure 7.1 demonstrate the complexity of the task and why different types of orbits will be damaging or benign. The prediction of solar particle event proton fluxes is more difficult, and present models are based on a probabilistic analysis involving mission duration and event confidence levels (Feynman *et al.*, 1992; Tranquille & Daly 1992). The high solar particle event doses in the lower energy range can be particularly damaging for spacecraft in eccentric or geostationary orbits (36 000 km) whereas spacecraft in low-inclination, near-Earth orbits (600 km) are protected from solar particle events by geomagnetic shielding effects.

The radiation belt models used in the analysis of the Hipparcos data are AE8 and AP8. AE8 (Vette 1991) is a model for the electron environment for energies of 40 keV to 7 MeV and altitudes of 1.2 to 11 Earth radii. Since solar activity can have a pronounced effect on the radiation environment experienced in an orbit the model comes in two forms. AE8MAX is appropriate for solar maximum conditions, while AE8MIN is for solar minimum. Similarly AP8 (Sawyer & Vette 1976) is a model of the trapped proton
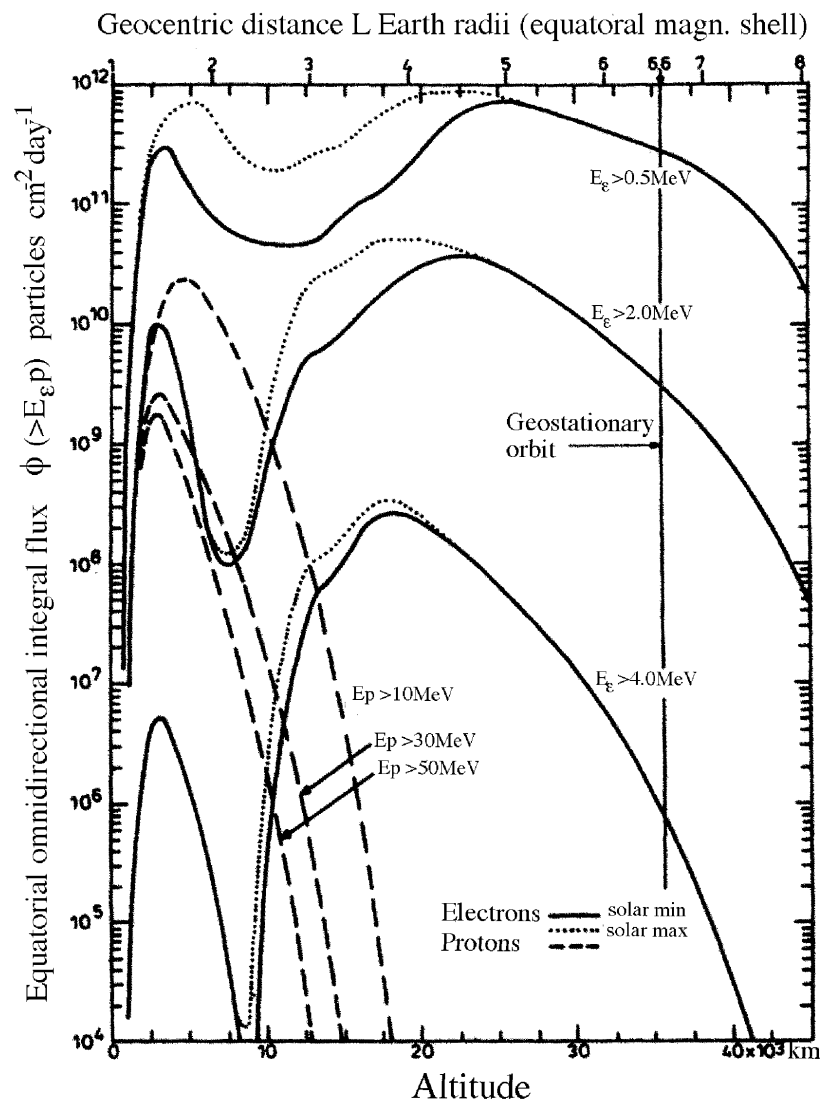
Figure 7.1. *The Earth's trapped electron and proton radial average flux profiles as a function of altitude (the Hipparcos satellite operated between 400 – 36 000 km). The different curves refer to different proton and electron energies (E_p and E_ϵ respectively). For electrons, the solid and dotted lines indicate the dependence at solar minimum and solar maximum respectively.*

environment for energies 100 keV to 400 MeV and altitudes of 1.15 to 6.6 Earth radii. This also has appropriate versions for solar maximum and solar minimum conditions.

An associated phenomenon—geomagnetic sub-storms—can lead to spacecraft anomalies and secondary solar-array damage. In this case occasional injections of hot plasma from the geomagnetic tail cause charging of surfaces to large negative potentials with respect to the surrounding plasma or different dielectric materials. Surfaces not neutralised by solar UV-induced photo-electron emission can develop large differential potentials leading to arc discharges. Electromagnetic interference from discharges is the cause of many anomalies on spacecraft and arcing can also damage exposed areas such as solar arrays. Special design features have to be incorporated to obviate this type of secondary damage and the associated electromagnetic interference.

Also troublesome are the solar eruptions producing energetic electrons, protons, α particles and nuclei such as C, N and O, although the most damaging components for spacecraft are typically protons. Galactic cosmic rays consist of approximately 90 per cent protons, 8 per cent α particles and 2 per cent nuclei of heavier elements. The energies are in the GeV range, but the fluxes are extremely low, around 2.5 particles cm^{-2} s^{-1}. However they are particularly penetrating and generate free charge in microelectronics, giving rise to single event upsets.

Protons

The energetic proton populations in space can be divided into three categories: (i) geomagnetically trapped radiation-belt protons with energies up to 300 – 400 MeV, which are primarily relevant for low-Earth and highly elliptic orbit missions; (ii) solar protons, notably those generated during a solar particle event. These may have energies from 10's to 100's of MeV, and occur sporadically. During a solar particle event, their fluxes can be extremely high. They tend to be deflected by the Earth's magnetic field (geomagnetic shielding) and thus pose a smaller threat to missions in low-Earth orbit. For missions with orbits outside the immediate vicinity of the geomagnetic shielding their effects can be crucial; (iii) protons originating from outside the solar system. These can be either galactic or extragalactic in origin. The galactic magnetic field can accelerate and contain protons with energies up to about 10^{19} eV, above which the particles are thought to originate outside the Galaxy. Such particles are extremely rare, such that they do not pose significant problems for satellites.

The daily positional proton flux encountered by Hipparcos is illustrated in Figure 7.2.

Electrons

In the vicinity of the Earth the largest contributor to the electron environment is the trapped radiation belt electrons, located in two zones: one at an altitude of $L = 1.6$ Earth radii, coincident with the proton belt, and an 'outer zone' at $L = 4.5$ Earth radii, where L is the geomagnetic dipolar field line equatorial radius. The largest electron fluxes are observed in the outer belt. Since the energy spectrum of trapped electrons drops exponentially, fluxes above 7 MeV are normally negligible. The dimensions of the two-component electron belt are much larger than those of the proton belt. The highest electron fluxes above the energy cutoff provided by typical spacecraft shielding are at least one order of magnitude higher than the respective maximum proton fluxes.

An important feature of the electron environment is its extremely dynamic nature. During disturbances, electron enhancements of several orders of magnitude can occur, and energies of tens of MeV have been observed. Current empirical models of the electron belts, however, consider the environment as static.

A population of high-energy electrons is also created during a solar flare. Due to the smaller magnetic rigidity of electrons, most of these remain trapped in the strong local solar magnetic fields—those that do obtain relativistic velocity and manage to escape lose much of their energy by emitting synchrotron radiation as they traverse the interplanetary magnetic fields. In the Earth's vicinity therefore the contribution to the high-energy radiation environment by solar flare originated electrons is very small. The same reasoning applies also to electrons arriving from outside the solar system.
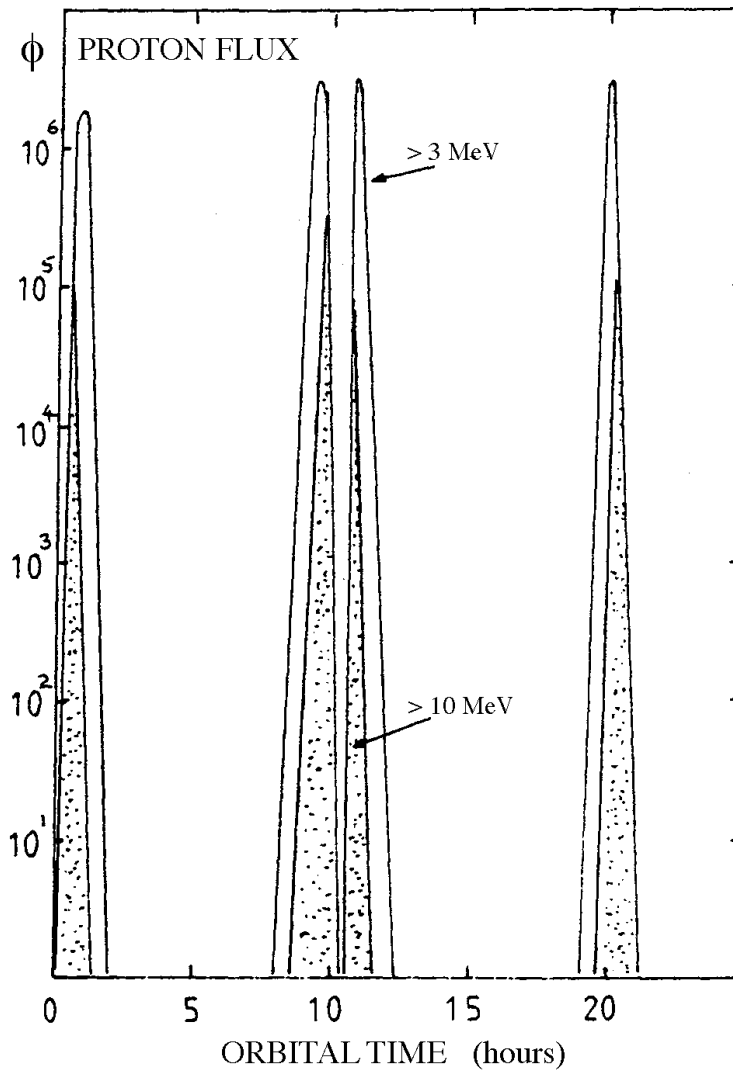
Figure 7.2. *The daily positional proton flux (in protons cm^{-2} s^{-1}) encountered by Hipparcos as it penetrated the van Allen belts four times per day in its elliptical orbit. The shaded regions correspond to the flux of > 10 MeV protons, and the open regions below the curves to > 3 MeV protons. Perigee passages correspond to the intervals close to 0 hrs and 10.7 hrs in the figure.*

Cosmic Ions

Cosmic ions also contribute to the charged particle environment in space, of which the most important are hydrogen and helium. The heavier nuclei are also of interest due to their high ionisation loss-rate in materials. There is also a small trapped heavy ion population in the radiation belts: the trapped anomalous cosmic rays. These particles in general tend to have low energies and consequently small ranges in matter compared to the equivalent shielding provided by most spacecraft, and are therefore of less interest from the radiation protection and monitoring point of view. However ions from outside the solar system, galactic cosmic rays, and accompanying solar particle events, are highly penetrating and deposit enough energy in sensitive nodes of microelectronic components to cause single event upsets or background.
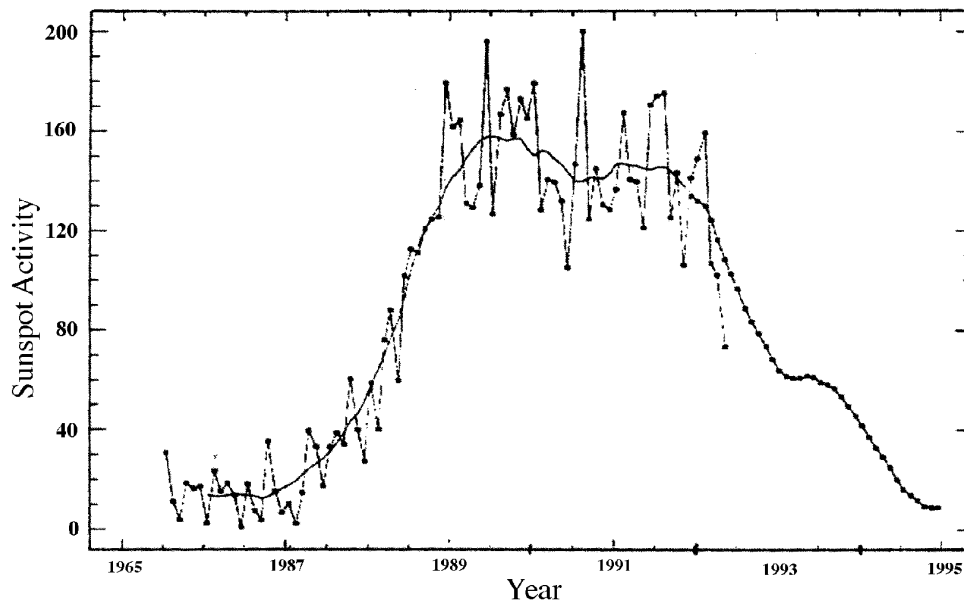
Figure 7.3. *Evolution of solar activity throughout the relevant solar cycle. The points give the monthly value of the sunspot number, the curve giving the smoothed values. The Hipparcos mission operated around the period of solar maximum.*

Solar Activity

Figure 7.3 shows the solar activity for the years preceding and during the Hipparcos mission. The solar maximum occurred during July 1989. After that the activity decreased. These determinations were made by the National Oceanic and Atmospheric Administration Center in Boulder, Colorado, U.S.A. In practice, Hipparcos was subject to three periods of intensive solar activity between the start of the mission and mid-1992—at the end of 1989, in the middle of 1990, and in the middle of 1991. Two exceptional solar proton events occurred in October 1989 and March 1991. The daily proton fluence is illustrated in Figure 7.4.

7.3. Modelling the Radiation Dose Absorbed by the Satellite

Following the implementation of the revised mission plan, studies were undertaken in an attempt to predict the future solar array performance as affected by the actual radiation background (see Chapter 11), and also the effects on the other spacecraft and payload electronics. This was carried out by comparing the effects of being in geostationary transfer orbit rather than its intended geostationary orbit using a simple scaling of the overall radiation dose levels. These studies resulted in a wide margin of uncertainty, but suggested that the electronic parts could withstand 32 months in the more severe environment.

Dose depth curves (Figure 7.5) were combined with a sector analysis to fit reality as close as possible. Sector analysis using a solid sphere dose depth curve corresponds to
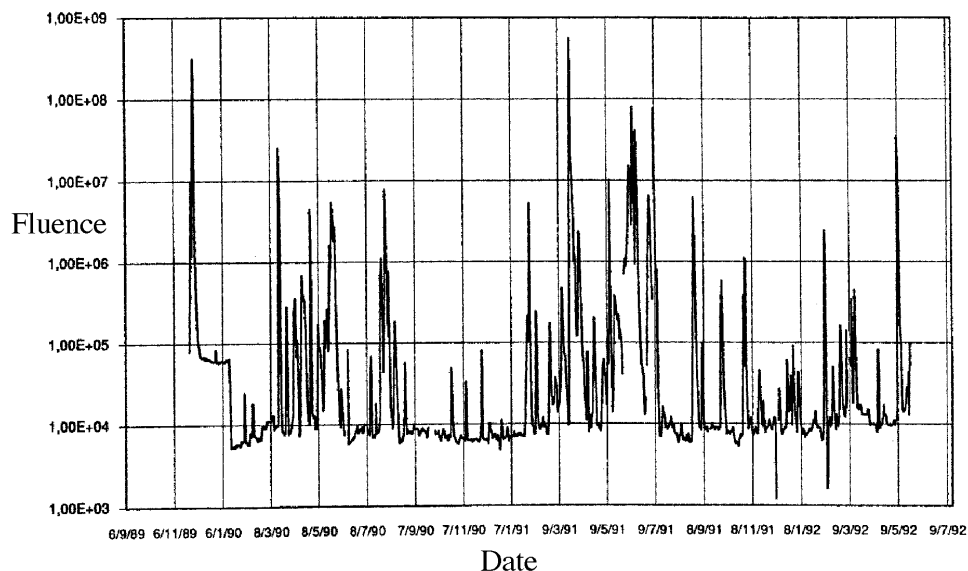
Figure 7.4. *Daily proton fluence during the mission, as indicated by solar activity reports communicated by the Observatoire de Paris-Meudon.*

an upper bound of total dose received, while sector analysis using a shell sphere dose depth curve corresponds to a lower bound but is closer to reality.

A margin of a factor of two had been applied when predicting the dose that a component could theoretically be exposed to, compared with its tested radiation hardness, meaning that the Hipparcos electronic parts were able to absorb at least twice the limiting dose specified for geostationary operation. Results are given in Figure 7.6, calculated for a 32 month mission according to the following two ratios:

$$\frac{\text{solid sphere dose}}{2 \times \text{specified geostationary dose}} \quad \text{and} \quad \frac{\text{shell sphere dose}}{2 \times \text{specified geostationary dose}}$$

The figure demonstrates that a significant divergence appears between the two extreme assumptions, depending on the equivalent aluminium thickness.

Another relevant aspect when interpreting various experimental data is the test conditions of components, particularly the dose rate used during irradiation tests. The dose rates in orbit are much lower than the testing dose rates, and experience in radiation testing shows that the behaviour of components under high dose rate conditions is worse than when using low dose rate exposures, except for a very few particular cases. This consideration gave an additional margin, difficult to assess quantitatively, which might also be expected to vary from one component to another.

For the studies of the radiation effects on the silicon solar-cell arrays, described in detail in Chapter 11, it was found to be desirable and possible to convert predicted integral proton and electron spectra outputs into a monoenergetic 1 MeV equivalent electron flux which, when time integrated, yields a 1 MeV equivalent electron dose flux (1 MeV electrons cm^{-2}). These flux values are readily and inexpensively simulated by van de Graaf accelerators, thereby enabling a solar cell's degradation characteristics to be assessed in the laboratory. The 'equivalence' concept holds good for penetrating radiation for which proton and electron irradiation produce the same qualitative solar-cell device degradation. The conversion of proton fluxes to equivalent 1 MeV electron
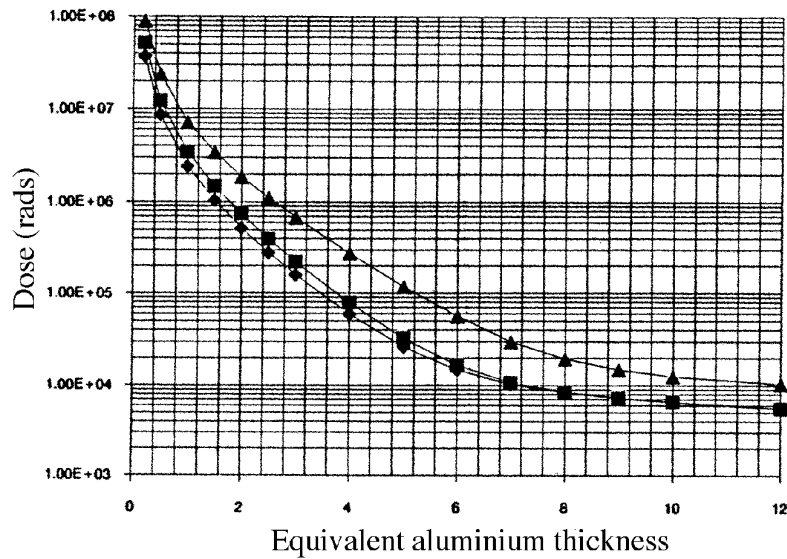
Figure 7.5. *Dose depth curves comparison for the actual Hipparcos orbit. Triangles and squares correspond to the dose curves for a solid sphere and a shell sphere respectively, the diamonds to two infinite slabs for comparison (see text for details).*
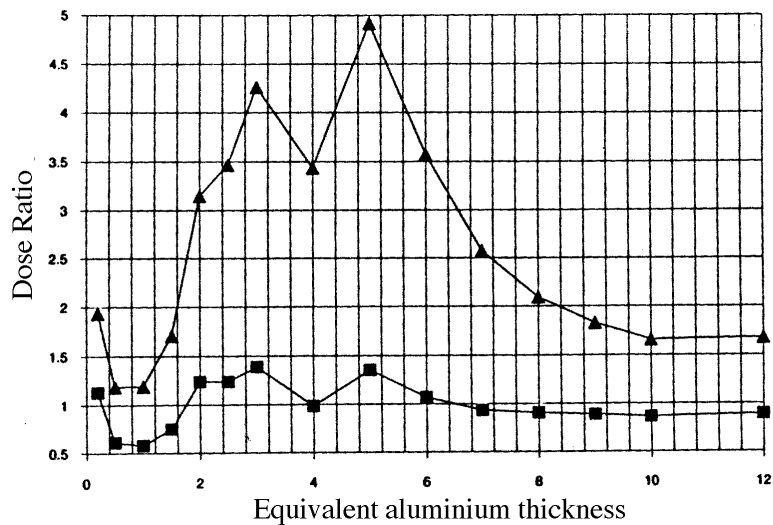

Figure 7.6. *Predicted dose ratio for a solid sphere (triangles) and a shell sphere (squares) with respect to twice the geostationary specified dose.*

fluxes is made by means of experimentally determined electron/proton damage ratio curves such as those depicted in Figure 7.7, from which it may be seen that 3000 1 MeV electrons are required to produce the same degradation as one 10 MeV proton in a 10 Ω cm n-p silicon solar cell. These proton-damage ratios are not universal constants, but have to be determined for each new type of silicon solar cell.
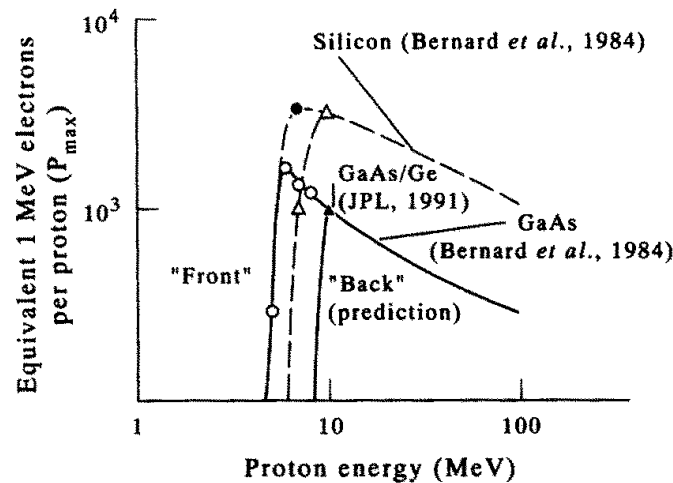
Figure 7.7. *Curves used to determine 1 MeV equivalent electron fluences as a function of proton energy. Different curves correspond to the effects of irradiation on the front and back sides of the panels (i.e. as a result of the shielding thickness). The curves permit the evaluation of the effects of orbital proton fluences in terms of equivalent 1 MeV electrons, and the subsequent testing of these cells using monoenergetic irradiation on ground. The 'silicon' curves correspond to the Hipparcos solar array, as used in the calculations described in the text. The GaAs/Ge relationships are shown for comparison.*

7.4. Effects of the Radiation Background on the Mission

Based on studies carried out before launch, the minimum shielding required to protect the sensitive spacecraft and payload components from radiation damage in the planned geostationary orbit was established to be equivalent to 8 mm aluminium. Particles penetrating normally (and therefore normal to the optical axis) retain most residual energy and are more numerous. This shielding corresponded to protons of about 40 MeV and electrons of roughly 3.5 MeV. However, electrons undergo considerable angular multiple scattering, and it is not possible to assign a unique penetration cut-off energy to them. Protons on the other hand travel in approximately straight lines. Near the end of their ranges they have a high linear energy transfer and a large contribution to the background signal is expected from fluorescence induced by protons within a few MeV of the penetration threshold.

Photomultipliers convert photon hits on a photocathode into an electrical signal via an amplified photo-electron cascade. Therefore radiation background signals can arise from: (a) secondary emission from photomultiplier window, cathodes or dynodes (internal electron-multiplying electrodes) induced by charged particle hits; (b) Cerenkov radiation in the spectral region of interest produced by charged particles passing through optical components (including the photomultiplier window); (c) fluorescence (scintillation) produced by charged particles in optical components; and (d) bremsstrahlung which can produce Cerenkov and fluorescence emissions via the generation of Compton-scatter electrons.

Secondary emission is most significant for low-energy particles. However, these are depleted in shielded situations. Secondary emission from the higher energy particles is generally inefficient compared to the other processes (Viehmann & Eubanks 1976).

Cerenkov radiation is a threshold effect requiring that the charged particle has a velocity exceeding the speed of light in the medium, which depends on refractive index. For most common glasses an electron need only have an energy above about 0.22 MeV to generate a Cerenkov flash. Protons on the other hand need energies above about 400 MeV. The direction relative to the particle track at which the light is emitted is a function of its velocity and the material's refractive index. A particle at the Cerenkov threshold velocity emits light in the forward direction while in common glasses the maximum emission angle, produced by highly relativistic particles, is about 45°.

Fluorescence is a continuous process with the amplitude of the photon emission dependent on the particle linear energy transfer. Photons are emitted isotropically. Even though the photon yield from an individual Cerenkov event may be larger than the yield from fluorescence, fluorescence may well produce the larger contribution. This is because of the very short duration and the directionality of Cerenkov emission, and because particles below the Cerenkov threshold can cause fluorescence.

Bremsstrahlung emission also has a significant angular spread. Although a Cerenkov event generates a large number of photons, the flash is extremely brief (100 ps) compared to the photomultiplier detection dead-time of 300 ns. A single Cerenkov event therefore only registers as a single count or 'spike' in the detector signal (Høg *et al.*, 1992; Howell & Kennel 1984; Viehmann & Eubanks 1976), and only the rate of Cerenkov events is registered.

Fluorescence is a much slower process lasting hundreds of micro-seconds and so contributes a larger count-rate. The slow rotation of the satellite and the fact that the planar shielding has its normal perpendicular to the rotation axis meant that over time the focal plane would view all directions. The rotation axis was in a sunward (but not exactly sun-pointing) direction so the rotation tended to expose the focal plane to most pitch angles (directions with respect to the magnetic field) over the 2 hour rotation.

Although the instantaneous environment seen by the telescope components had a directionality, time-averages and the large acceptance angle tended to make the response more isotropic. In the cases of electrons and bremsstrahlung, their multiple scattering and angular distributions further blurred directional effects.

In-Orbit Measurements

The 'star mapper chains' consisted of a series of 5 lenses, 2 filters and a pair of Thorn-EMI 9924B photomultiplier tube detectors. These detectors were specially built with thin windows to minimize Cerenkov radiation and fluorescence. Shielding of the Hipparcos focal plane star mapper optical components was approximately planar. The optical axis lay in a plane parallel to the plane of the shielding.

Figure 7.8 shows typical traces of the star mapper signal during four sequential orbits. The vertical lines indicate the times of perigee. Close to perigee the background signal is extremely high, corresponding to the inner, proton, radiation belt. The broad peaks of the electron belts on the outbound and inbound passages are apparent. As part of normal operations the instruments were shut down or data rejected during periods of
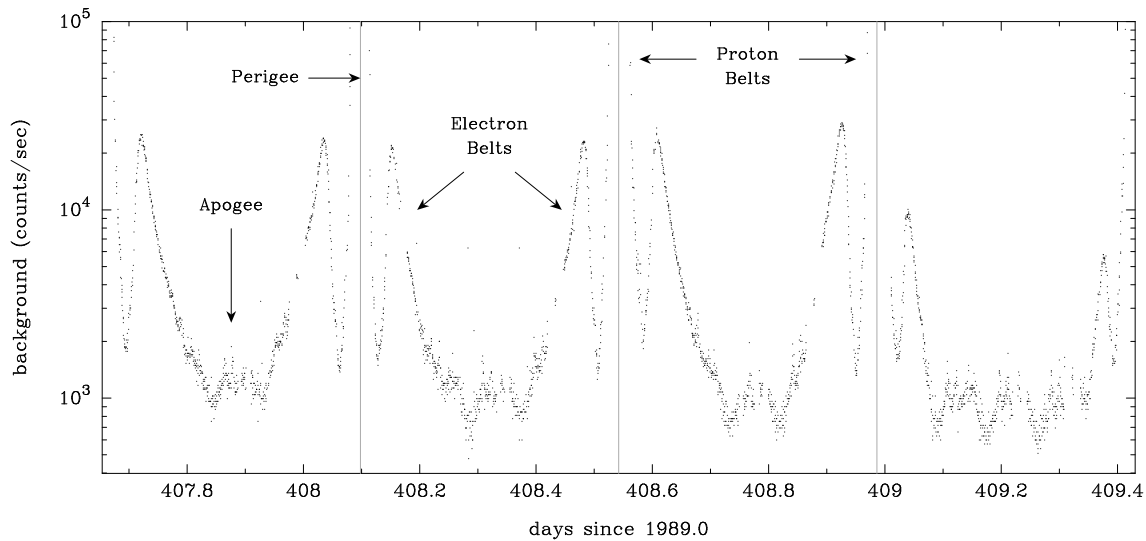
Figure 7.8. *Typical star mapper orbital background signal over a period of about 2 days. The vertical lines indicate the location of the perigee passages. The minima in the background signal correspond to the apogees of the orbit.*

very high background signal. Some data outages were also due to on-board anomalies which may themselves have been environmentally induced. Data were also not taken when the Earth or Moon were in the star mapper fields of view. Nevertheless, there were enough data in high-background regions to reveal clearly many interesting features. The background signal data consisted of 1000 points equally spaced in time per orbit, giving a resolution of about 38 s. The data set started close to the start of scientific operations, on 26 November 1989 and finished more than 3 years later on 17 March 1993, totaling 2722 orbits. Gaps totalled about 18 per cent of this time and were concentrated towards the end of the mission.

Interpretation of the Data

The data can be displayed as plots in terms of orbital time for various periods of interest. Figure 7.9 shows data for 20 orbits (9 days) of late March 1991. Also plotted on this figure are data from the particle detectors on the geostationary GOES satellite (Sauer 1987). These are for electron fluxes (cm^{-2} s^{-1} sr^{-1}) > 2 MeV divided by 10^3 and for proton fluxes (cm^{-2} s^{-1} sr^{-1} MeV^{-1}) of 11.6 MeV divided by 10 and of 60.5 MeV (the scaling is solely to fit the data in the figure). These GOES data show the onset of the well-known solar proton event on 23 March 1991 (Mullen *et al.*, 1991; Gussenhoven, Mullen & Violet 1994). The subsequent solar wind shock on 24 March resulted in the creation of an additional radiation belt (Blake *et al.*, 1992). The solar proton event is clear in the dramatically enhanced Hipparcos star mapper background signal rate. Also apparent is the dramatic fall in rate as perigee approaches, presumably due to geomagnetic shielding. This event also generated strong electron and proton drift
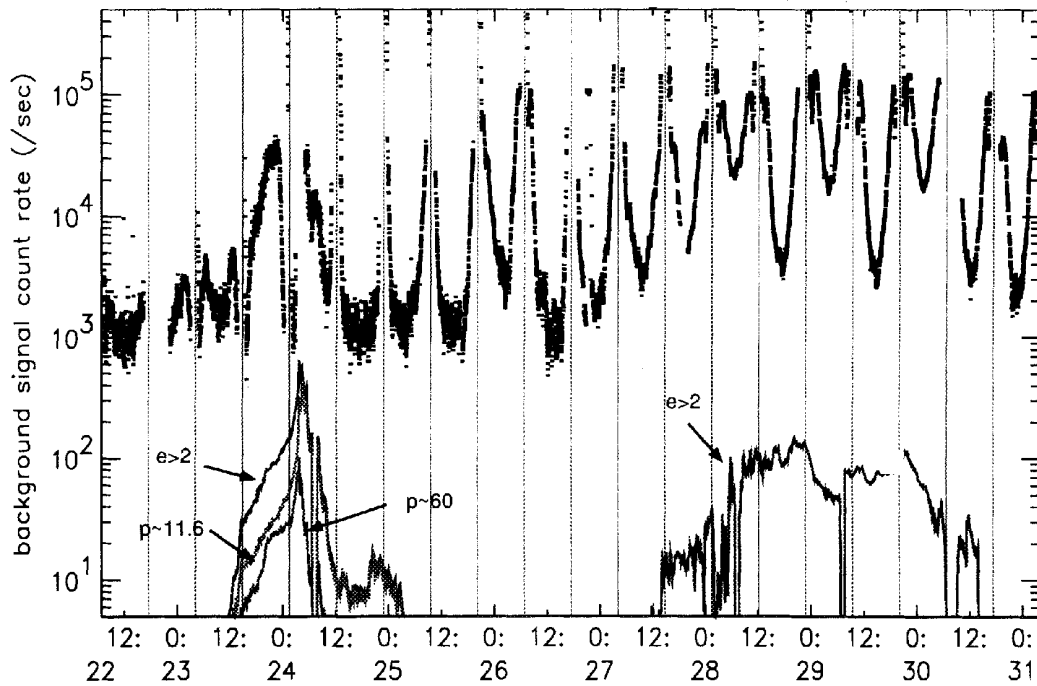
Figure 7.9. *Hipparcos star mapper background signal data for 20 orbits during late March 1991 (upper trace). The vertical lines indicate the periods of perigee passage: the star mapper background usually decreasing as the satellite altitude increases towards apogee. At the bottom of the figure are the corresponding GOES electron and proton data (scaled as described in the text). At the lower left, the three traces show the response to a large solar proton event, the three curves corresponding to electrons with energy above 2 MeV (upper), protons above 11.6 MeV (middle), and protons above 60 MeV (lower). To the bottom right of the figure are the GOES data corresponding to the subsequent geomagnetic storm (the curve is for electrons above 2 MeV) giving rise to a 1–2 order of magnitude increase in the star mapper background count rate.*

echoes at around 3:42 UT on 24 March (Blake *et al.*, 1992). Unfortunately the star mapper data for around this period are missing due to ground-station non-availability.

Earth occultation results in the absence of any inner-belt traces on the orbits shown in Figure 7.9, in contrast to Figure 7.8. On the orbits following 27 March an additional maximum is clearly seen, corresponding to the new belt and coincident with the enhancement of the GOES > 2 MeV flux shown at the bottom of the figure. A feature of the response in the days following 27 March is the way the background signal at 6 successive apogees 'oscillates' by close to an order of magnitude while the new belt magnitude and the GOES fluxes remain relatively stable. This is presumed to be a longitude effect caused by the tilt of the geomagnetic field; as the Earth rotates, successive orbits trace different paths through the geomagnetic field.

To relate the data better to radiation belt regions they were analyzed in terms of location in geomagnetic L space rather than time which compresses the lower altitude. The time of the data was used together with orbital ephemeris data to derive the L value corresponding to every data point. To do this the IGRF-1985 (International Geomagnetic Reference Field) model of the Earth's internally generated magnetic field was used together with the Olsen-Pfitzer-1977 quiet-time tilt-dependent model of the externally generated perturbation (Olsen & Pfitzer 1974) to compute B (the magnetic field strength) and L. This is the same procedure that has been used to order data from the

Combined Release and Radiation Effects Satellite (CRRES, Gussenhoven *et al.*, 1992; Brautigam, Gussenhoven & Mullen 1992). Since the orbit is of low inclination, L alone should produce reasonably good ordering of the data. However, as mentioned above, the tilt of the geomagnetic field and the $7°$ inclination combine with the Earth's rotation to produce a shift between orbits in L space. In other words subsequent apogees will not lie on the same L value. Around apogee, different orbital traces which were well ordered (overlapping) in orbital time were sometimes less well ordered when traced in L, indicating that the model fields were inadequate at high altitudes. At low altitudes, organising the data according to L was very effective at revealing the belt structures, even with patchy data. L distributions of the data for each orbit were derived by averaging the data in bins of 0.05 Earth radius in L. The complete mission background signal data and their temporal and L distribution are summarized in Figure 7.10. In this figure, as with other authors' method of plotting CRRES data summaries (Gussenhoven, Mullen & Violet 1994; Brautigam, Gussenhoven & Mullen 1992), the counts are displayed as a colour-scale with the vertical axis corresponding to the radial L variation (the bottom of the figure, $L = 1$, can be thought of as approximately the Earth's surface) and the horizontal axis corresponding to time, covering more than 3 years of data. To condense the plot and in order to remove residual longitude effects, the single-orbit L-distributions were averaged in 9-orbit segments, corresponding to the repeat period of 4 days. Just over 300 data segments are displayed horizontally, and there are 115 L bins within each segment.

The figure clearly illustrates the quiet period from September 1990 until the March 1991 event, the subsequent generation of the new radiation belt around $L = 2$, and the large event of July 1991 which was reported to remove some of the new belt (Gussenhoven, Mullen & Violet 1994).

This behaviour was also registered in the Hipparcos solar array degradation, which degraded at an unusually slow rate just before the March event and at a fast rate afterwards (Crabb & Robben 1993, see also Chapter 11). The Hipparcos data with its longer time-coverage also captured the events of April 1990, November 1991 and, largest of all, May 1992. The April 1990 event is seen to add slightly to the edge of the inner belt for a period of about a month. The November 1991 event produced a distinct narrowing of the second belt. The large May 1992 event, however, produced little lasting effect on the inner belt or the second belt which had all but decayed away by then.

Comparison with CRRES dosimeter data supports the view that both electrons and protons produced the background signal: the signal was strong in the inner belt below $L = 1.5$; it was temporarily very strong in the second inner ($L \simeq 2$) belt following the March 1991 event but subsequently decayed; and it responded readily to electron events seen by other spacecraft. In the CRRES data there is less obvious decay of the HiLET second belt (in the region $2 < L < 2.5$) than the LoLET second belt while the Hipparcos second belt decays noticeably. This would imply that protons are less important. However, the inner belt shows up stronger in the Hipparcos data than in the LoLET data. From this it appears that in this region Cerenkov radiation from very energetic protons is becoming an important component, while at higher altitudes, electrons and bremsstrahlung are the main contributors.

Because inner zone protons capable of generating Cerenkov radiation are of very high energy, the shielding around the telescope was largely ineffective. These protons therefore could access the telescope from a much greater range of directions. Using the

Colour figure to be inserted here

Figure 7.10. *The L-distribution of the Hipparcos background signal over most of the mission showing several solar proton events, and the creation and decay of the second inner belt around L = 2 around March 1991. The data are a 4-day (9-orbit) average, binned in 0.05 R_E in ordinate. The red regions for L > 3 (corresponding to the outer electron belt) arise from injection events.*
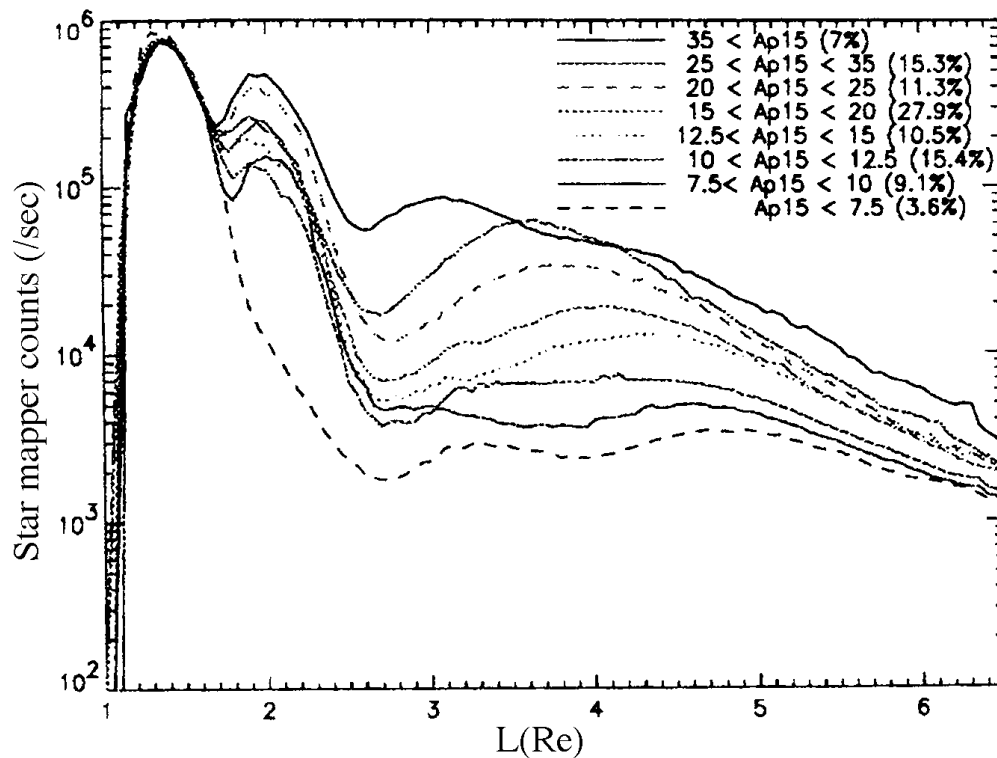
Figure 7.11. *Average radial L profiles of the star mapper background for various geomagnetic activity levels. It shows an increasing background trend for increasing value of the planetary A_P geomagnetic index. The percentages in parentheses indicate the fraction of the mission duration for the given index value.*

orbital *L*-binned data, average *L*-profiles of the background signal under various geomagnetic activity conditions were produced. The activity conditions were defined by the 1-day delayed 15 day average of the planetary A_P geomagnetic index available from the National Oceanic and Atmospheric Administration (NOAA), denoted A_P15. This scheme had previously been successfully applied to the sorting of CRRES high energy electron data (Brautigam, Gussenhoven & Mullen 1992).

Figure 7.11 shows the resulting activity ranges and in brackets the percentages of the total data which fall into each activity category. The lowest activity category corresponds to an almost total absence of an electron radiation belt ($2.5 < L$). There is a strikingly clean signature of the inner proton belt ($L \simeq 1.5$). The second inner belt ($L \simeq 2$) is also clear under higher activity conditions which are dominated by periods after March 1991. The lowest activity class is dominated by pre-March 1991 conditions, explaining the absence of the second inner belt. This type of geomagnetic activity separation is most useful for the outer regions since clearly perturbations to the inner regions persist during times of high and low geomagnetic activity. Beyond $L = 3$ there is a clean monotonic increase with A_P15 in the electron-induced background signal, most similar to the medium-energy models ($2.2 - 3.1$ MeV) of Brautigam, Gussenhoven & Mullen (1992).

Although there can be no real substitute for direct and unambiguous particle measurements for defining the environment, a by-product of the satellite's unplanned operation in geostationary transfer orbit was a long-term set of radiation background data giving

information on the radiation environment in important orbital regimes. These data are interesting in a number of respects. Comparison with data from an overlapping time period from CRRES facilitates the deduction of the cause of many elements of the background signal's spatial and temporal dependence. As with previous CRRES results, the data illustrate the highly dynamic nature of the electron component of the radiation environment. They show how the geostationary transfer orbit environment, thoroughly monitored for 14.5 months by CRRES, behaved in the 6 months before and 12 months after CRRES. In particular the long-term decay of the second inner ($L \simeq 2$) belt following the March 1991 event is seen, the very large event of May 1992 produced negligible effect on the belt structure and the November 1991 event produced a distinct loss from the second belt. Qualitatively, Hipparcos data and CRRES data are consistent during the overlapping period, especially the LoLET dosimeter in the outer zone and the secondary inner belt.

Comparison with GOES data following the March 1991 event reveals some interesting features at high altitudes in the background signal data related to geomagnetic field effects. In the inner parts of the orbit there was interesting evidence of geomagnetic shielding of solar proton events. While it is not possible to identify a unique particle species or detection mechanism, it is reasonable to conclude that the signal is from Cerenkov radiation and fluorescence caused by electrons, protons and bremsstrahlung.

In conclusion, although the geostationary transfer orbit environment can be a severe one, it has its quiet moments. It was never seriously contemplated to perform space-based astronomy from geostationary transfer orbit but these data and the eventual success of the Hipparcos mission show that it is feasible under certain circumstances. The possibility of operating in orbits which are normally considered too hazardous for spacecraft has obvious cost benefits, provided the protection aspects can be managed. These data are highly relevant for ESA's future space-based astronomy missions which will take place in highly-eccentric Earth orbits. They should yield important statistics for observation planning. They should also provide an interesting additional geostationary transfer orbit data set to add to those from CRRES. Finally they demonstrate the suitability of geostationary transfer orbit for radiation-belt and solar-terrestrial studies.